Three-Dimensional SPECT Simulations of a Complex Three-Dimensional Mathematical Brain Model and Measurements of the Three-Dimensional Physical Brain Phantom

Hee-Joung Kim, Barry R. Zeeberg, Frederic H. Fahey, Alden N. Bice, Edward J. Hoffman, and Richard C. Reba

Department of Radiology, George Washington University, Washington, DC.; Georgetown University, Washington, DC.; University of Washington, Seattle, Washington; and UCLA Medical School, Los Angeles, California

We have developed a three-dimensional computer simulation of SPECT imaging. We have applied the simulation procedure to the realistic mathematical Hoffman three-dimensional brain model to generate the projection data (in the absence of attenuation, scatter, or noise) of both a parallel-hole and a multidetector SPECT system with point-focusing collimators. The simulated projection data were then reconstructed using standard software. The projection data resulting from the distribution of grey matter alone, or grey and white matter, were simulated. The results of these simulations indicate the existence of significant qualitative and quantitative artifacts in reconstructed human brain images. For example, the reconstructed values for grey matter along a cortical circumferential profile in a transverse slice through the basal ganglia varied by a factor of 2.40 (parallel-hole) and 2.99 (point-focusing), although the original grey matter values were identical in all cortical regions in the model. We have compared the simulated reconstructed images with those obtained by imaging the physical three-dimensional Hoffman brain phantom, which was constructed based upon the same set of data from which the mathematical three-dimensional Hoffman brain model was derived. Although the simulation did not include all of the degrading factors present in the physical imaging, the two images were in good agreement, indicating the applicability of the simulation to a realistic situation and the importance of the detector resolution effect.

J Nucl Med 1991; 32:1923–1930

Using the muscarinic acetylcholinergic receptor (mAChR) binding radioligand (R,R)-[^{123}I]4IQNB and a multidetector point-focusing SPECT instrument, we have found apparent deficits in the posterior parietal cortex in normal volunteers and in Alzheimer's disease patients (*1*, *2*). These apparent deficits may be due to altered radioactivity localization or to imaging/reconstruction artifacts.

The quantitative potential of SPECT or PET for estimating the regional concentration of neuroreceptors or blood flow can be degraded by inaccuracies in kinetic modeling of radiotracer localization, as well as inaccuracies in image reconstruction. In particular, a shape- and size-dependent recovery coefficient (*3*) could cause two regions with identical radioactivity concentration artifactually to appear to have significantly different radioactivity concentrations. For example, this phenomenon would be troublesome in the case of the muscarinic cholinergic receptor, which is distributed uniformly throughout the grey matter of the cerebral cortex (*4*). In this case, there may be an apparent regional difference of radioligand localization caused by differing regional thicknesses of cortical grey matter.

We have previously reported the results of computer simulation studies using a multi-detector point-focusing SPECT instrument and the grey matter distribution within a brain slice cylinder (*5*,*6*). We now extend those studies by: (a) including simulations using an ultra high-resolution parallel-hole SPECT instrument; (b) using the mathematical three-dimensional Hoffman brain model (*7*); (c) simulating grey and white matter in addition to grey matter alone; and (d) imaging the physical three-dimensional Hoffman brain phantom that was constructed based upon the same set of data from which the mathematical three-dimensional Hoffman brain model was derived (*7*).

MATERIALS AND METHODS

Imaging Physical Phantom

A physical Hoffman three-dimensional brain phantom with a grey-to-white matter ratio of 5:1 (*7*) was filled with approximately 15 mCi (555 MBq) of ^{99m}Tc in 1400 ml of water, taking care to avoid introducing air bubbles. The phantom was scanned 4 hr after filling using the Trionix Triad three-headed camera with a set of ultra high-resolution parallel-hole collimators, and 7 hr after filling using the Strichman 810 with a set of 572 hole point-focusing collimators. A description of the physics of point-focus-

Received Jan. 2, 1991; revision accepted Apr. 2, 1991.

For reprints contact: Barry Zeeberg, PhD, Department of Radiology, Radiopharmaceutical Chemistry, Room 662 Ross Hall, 2300 I St. NW, Washington DC 20037.

ing instrumentation has been given previously (*5,6,8*). The acquisition parameters for parallel-hole collimators are 13.6 cm rotational radius, 15% energy window, 120 angular views, approximately 0.23×10^6 counts/slice, 64×64 array with 3.56 mm pixel^{-1} for the projection data. Those for point-focusing collimators are 20% energy window, 2.5×10^6 counts/slice, 20 slices, 12 lines, and 6 mm slice spacing.

For the parallel-hole collimators, the measured projection data were reconstructed by filtered backprojection in the spatial domain using a Hamming filter with cutoff frequency 0.43 pixel^{-1} and corrected for attenuation with Chang's first-order correction method (*9*) by using the circular boundary of the physical Hoffman three-dimensional phantom. For point-focusing collimators, the measured projection data were reconstructed with the manufacturer's reconstruction software (version 2.51) using the relatively high-resolution filter which we previously determined to be optimal for human imaging systems (*6*). These filters are proprietary, and no information is available about their design. Attenuation correction was applied using the manufacturer's software with an "absorption length" equal to 60 pixels (*10*).

Detector Response Characteristics

For point-focusing collimators, the three-dimensional point spread function (3DPSF) was experimentally measured as previously described (*6*). *The 3DPSF represented the projection data, not the reconstructed image*, and was normalized so that the integrated volume was equal to unity.

For parallel-hole collimators, the 3DPSF was experimentally measured using a line source: polyethylene tubing (1 mm i.d., 28 cm length) was filled with a ^{99m}Tc solution (15 mCi (555 MBq) in 0.2 ml) and the ends of the tubing thermally sealed. The tubing was secured on top of a flat surface as a straight line source. The camera face was positioned at several distances from the source, zero to eight plexiglas sheets ($1.3 \times 23 \times 23$ cm) were positioned between the line source and the detector, and the source was imaged for 2 min. The line source was imaged using the Triad SPECT system. The acquisition parameters were: 15% energy window, 128×128 array with 1.11 mm pixel^{-1} for the projection data. The acquired data were decay- and attenuation-corrected.

The averaged profile perpendicular to the line source was analyzed as the sum of three Gaussians using an iterative nonlinear least squares curve fitting program. Relative, rather than absolute, residual errors were used in the curve fitting procedure in order to fit adequately the low amplitude tails. The parameters to be fit were the amplitude (A), sigma (σ), and center of each Gaussian. The first Gaussian represented the geometric detector response, and the second and third Gaussians represent the components due to scatter within the plexiglas, septal penetration, and scatter within the crystal. A and σ for all three Gaussians could be modeled as functions of the distance between the line source and the detector face and the depth of the plexiglas scattering medium. Only the first Gaussian, which represented the geometric detector response, is used in the simulations presented here, and A and σ for this component could be modeled as a function of the distance (D) between the line source and the detector face and the depth (d) of the line source within the scattering medium (A = 2,094 counts − 4.957 counts/mm D; for 0 mm $\leq$ d < 39 mm, σ = 1.407 mm + 0.01298 D + d ($-9.667 \times 10^{-4} + 4.312 \times 10^{-5}$D), and for 39 mm $\leq$ d < 250 mm, σ = 1.369 mm + 0.01466 D), for D $\leq$ 250 mm, where D and d are given in mm. For comparison, at D = 130 mm, for the second Gaussian A = 8.57 counts, and σ = 10.24 mm; and for the third Gaussian A = 1.75 counts, and σ = 49.86 mm. The sigmas for both the response from the line source and from the point source would theoretically be the same; however A for the response for the point source must be computed from the formula: $A_{PSF} = A_{LSF}/(\mathrm{sqrt}(2\pi)\sigma_{LSF})$ (see Appendix).

These formulas for A and σ are derived from measurements of a 1-mm line source and can be used in simulations in which the object resolution is 1 mm (see Results, section 1). For simulations in which the object resolution is 3 mm, the appropriate formulas for A and σ were derived by analysis of the projection data resulting from simulations of a 3-mm cube: a mathematical model of a 3-mm cube was prepared by packing together twenty-seven 1-mm voxels. The projection data were simulated at a series of distances between the cube and the detector, as done for the brain simulation shown in Figure 2, except only one fixed angular view was simulated. The projection data at the different distances were analyzed in a manner identical to that described above for the 1-mm diameter line source, except that A_{PSF} was determined directly rather than using the formula: $A_{PSF} = A_{LSF}/(\mathrm{sqrt}(2\pi)\sigma_{LSF})$. In order to facilitate comparison with the formulas given above for the 1-mm line source, however, we present the formula for A_{LSF} using the inverse relationship $A_{LSF} = A_{PSF}(\mathrm{sqrt}(2\pi)\sigma_{LSF})$: A = 51071 counts − 111.23 counts/mm D; for 0 mm $\leq$ d < 39 mm, σ = 1.5596 mm + 0.012611 D + d ($-1.0987 \times 10^{-3} + 4.1941 \times 10^{-5}$D), and for 39 mm $\leq$ d < 250 mm, σ = 1.5156 mm + 0.014289 D.

Imaging Simulation Studies

The in-slice resolution of the digitized mathematical Hoffman brain model is 1 mm × 1 mm with 6-mm interslice spacing. We were able to represent the model using cubic voxels of 1 × 1 × 1 mm, so that a slice in the original model would be 6 voxels in thickness. For all the isolated slice simulations, we utilized a slice of 1 voxel thickness. In order to represent the three-dimensional brain model at a voxel resolution of 3 mm × 3 mm × 3 mm, we sampled every third voxel within the transaxial slice, and then duplicated and extended each transaxial slice to an axial length of 2 voxels.

The simulated projection data are built up as the successive summation of projection data for each nonzero voxel: for each nonzero voxel, the measured 3DPSF is multiplied by the voxel value, translated according to the voxel position, and summed into an array containing the accumulated simulated projection data. Symbolically, a nonzero voxel at position (i,j,k) contributes OBJ(i,j,k)3DPSF(i′-i,j′-j,k′-k) to PROJ(i′,j′,k′), where PROJ is the simulated projection data and OBJ is the mathematical radioactive object. This computation is object-driven. For parallel-hole simulations, we used a modification in which an analytical expression for the 3DPSF was used in place of tabulated measured numerical data. For simulations which included both grey and white matter, two separate simulations were performed, and the projection data added together in a ratio of 5:1 to simulate the 5:1 ratio in the physical phantom. (*7*).

For point-focusing collimators, the simulated projection data were converted to the format required by the manufacturer's reconstruction software. The simulated projection data were reconstructed. The same filter used for the physical phantom was applied in the simulations. The reconstruction algorithm automatically performs a background subtraction based upon the radioactivity detected in certain positions of the projection data.

For parallel-hole collimators, we applied the same filter used for the physical phantom. Since the simulation studies did not include the effect of attenuation, we did not apply an attenuation correction to any of the simulated projection data.

Data Analysis

Regions of interest (ROIs) were drawn using the theoretical maps of grey matter (Fig. 1B), white matter (Fig. 1C) or ventricles (not shown). Circumferential cortical profiles were determined as described previously (*5,6,11*), using the circumferential path drawn on the theoretical map of grey matter (Fig. 1D). A circumferential profile was obtained by tabulating the counts in pixels along a circumferential path chosen manually so as to lie entirely within cortical grey matter pixels, approximately parallel to the exterior outline of the cortex. Approximately 30 control points are interactively selected, and these are automatically connected by straight line segments. Approximately 85 pixels along the straight line segments are sampled programmatically and the counts are plotted against the distance along the path.

Data obtained using circumferential profiles were normalized such that their mean is equal to unity. Data obtained using the ROI template (Table 1) were normalized by several methods:

1. Data in columns 1 and 2 were scaled separately so that the maximum was equal to 100. Then data in columns 3–4 were scaled by the same scale factor used for column 1. The same procedure was repeated for columns 8–10.
2. Data in individual columns 5 and 6 were normalized so that the maximum value was equal to 100.
3. Data in columns 7 and 11 were normalized so that the mean values for the grey matter regions were equal to the mean values for the grey matter regions in columns 4 and 10, respectively, for the purpose of comparison with the simulated data in those columns.

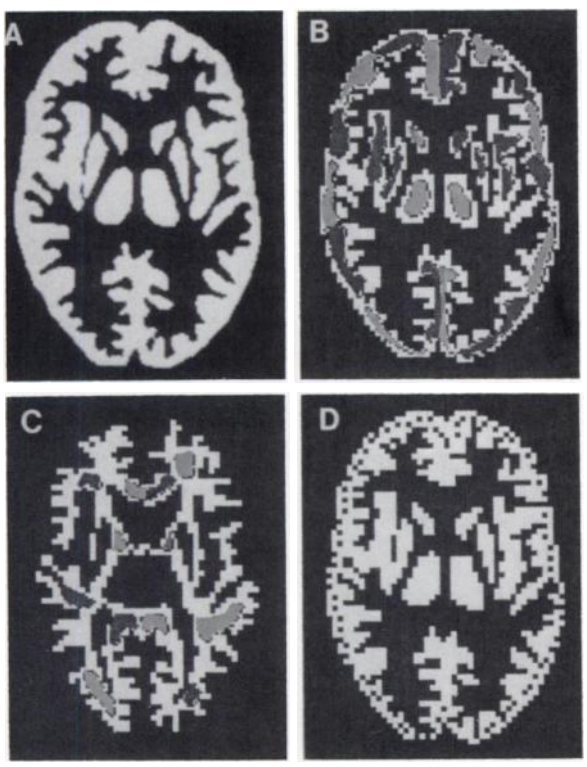

FIGURE 1. Digitized transverse slices through the basal ganglia chosen from the three-dimensional Hoffman brain model (7), indicating ROIs or circumferential path. Grey matter with 1-mm voxels (A), grey matter with 3-mm voxels with ROIs used in analysis superimposed as greyish regions (B), white matter with 3-mm voxels with ROIs used in analysis superimposed as greyish regions (C), and grey matter with 3-mm voxels with black dots indicating the location of the circumferential path (D). For ROIs, two grey levels are used in order to facilitate visually distinguishing adjacent regions of interest.

TABLE 1
Region of Interest Analysis for the Simulated and Physically Measured Hoffman Three-Dimensional Brain Phantom

COLUMN #	1	2	3	4	5	6	7	8	9	10	11
	PH							PF			
Dim and Matter	2DG	2DG	3DG	3DGW	2DG	2DG	Mean	2DG	3DG	3DGW	Mean
Object(mm)	3	3	3	3	1	3					
Sampling(mm)	3	3	3	3	1	1	3.56				
Angles(#)	64	128	64	64	64	64	128				
REGION	Fig 3	Fig 5	Fig 7A	Fig 7B	Fig 2	**	Fig 6	Fig 10	Fig 12A	Fig 12B	Fig 13
LMFC	87	85	267	277	95	91	314	85	685	620	756
LAFC	76	76	228	228	76	80	251	60	375	396	649
LPFC	81	83	234	241	77	86	251	74	485	497	548
LTC	85	85	246	253	86	85	254	81	605	508	553
LPTC	90	90	239	250	84	91	228	70	435	474	323
LPC	85	85	246	254	82	83	239	85	584	586	525
LPPC	82	83	210	218	85	77	226	74	392	409	490
LOC	87	88	230	247	90	85	258	73	522	540	699
ROC	89	90	237	263	87	93	248	82	566	585	665
RPPC	68	67	192	207	73	71	214	54	360	392	402
RPC	98	98	268	275	93	99	240	98	613	631	474
RPTC	86	88	243	248	83	87	214	74	482	506	372
RTC	88	88	248	253	86	90	231	88	612	615	488
RPFC	87	87	242	250	89	80	247	75	488	515	565
RAFC	83	85	241	249	83	83	260	74	474	492	608
RMFC	100	100	281	289	93	100	319	100	702	696	822
LINS	91	90	219	239	90	89	237	80	470	525	498
LCD	66	65	138	156	67	68	177	50	296	346	286
LPUT	69	69	149	182	72	68	198	54	312	409	363
LTH	98	98	218	231	100	100	204	93	433	480	422
RINS	92	91	217	237	92	91	239	82	441	508	509
RCD	61	57	141	154	67	70	152	41	311	341	302
RPUT	82	82	194	219	85	78	228	61	362	448	437
RTH	98	96	206	219	96	95	200	88	422	482	405
LGCC	6	7	32	61	9	3	131	-3	107	206	210
LACS	5	7	34	90	6	2	143	-4	38	168	161
LGIC	31	32	95	132	24	34	175	20	216	316	351
LOR	11	12	66	115	6	12	169	1	184	289	226
LPCS	16	17	61	109	8	16	161	1	128	240	223
LSCC	9	9	20	69	5	7	131	-2	134	219	321
RGCC	14	14	41	87	7	18	133	3	168	257	316
RACS	9	9	46	98	8	5	150	3	121	239	241
ROR	14	13	78	125	8	7	196	9	237	346	319
RGIC	24	29	87	123	25	16	169	16	227	308	319
RPCS	19	21	39	97	14	16	156	2	33	167	148
RSCC	13	14	59	106	11	8	178	-3	140	237	352
LAHLV	14	15	34	41	7	18	110	4	124	150	158
V III	19	24	42	56	12	18	101	13	205	242	239
LALV	3	3	12	49	8	3	114	-8	5	86	134
RALV	2	2	9	39	-1	5	120	-6	-14	45	36
RAHLV	14	14	27	39	15	5	114	-1	81	114	101

Abbreviations:
Grey matter: MFC-medial frontal cortex, AFC-anterior frontal cortex, PFC-posterior frontal cortex, TC-temporal cortex, PTC-posterior temporal cortex, PC-posterior cortex, PPC-posterior parietal cortex, OC-occipital cortex, INS-insula, CD-caudate nucleus, PUT-putamen, TH thalamus, White matter: GCC-genu of corpus callosum, ACS-anterior centrum semiovale, GIC-genu of internal capsule OR-optic radiations, PCS-posterior centrum semiovale, SCC-splenium of corpus callosum Ventricle: AHLV-anterior horn of lateral ventricle, V III-ventricle III, ALV-atrium of lateral ventricle
G-Grey matter, GW-Grey and White matter

** Data from a simulated reconstructed image of grey matter in an isolated basal ganglia slice imaged with a PH 3 mm and 1 mm resolution were used for the object and projection data sampling, respectively, and 64 angular views were utilized. (Fig. not shown)

RESULTS

Resolution of Brain Model Representation and of Sampling

Visual comparison of the brain model grey matter (Fig. 1A), with a simulated isolated slice parallel-hole reconstruction of this same grey matter with 1-mm resolution for the projection data and 64 angular views, in the absence of attenuation, scatter, or noise (Fig. 2), indicates the high degree of performance of this system. In order to decrease the computational requirements for subsequent three-dimensional simulations, the brain model was represented at $3 \times 3 \times 3$ mm resolution (Fig. 1B), with 3-mm resolution for the projection data and 64 angular views. Visual comparison of the reconstruction of the grey matter with 3-mm resolution for the projection data and 64 angular views (Fig. 3) with that obtained at the higher resolution

FIGURE 2. Simulated reconstructed image of grey matter in an isolated 1-mm thick basal ganglia slice imaged with parallel-hole collimators. One-millimeter resolution was used for the object and projection data sampling and 64 angular views were utilized.

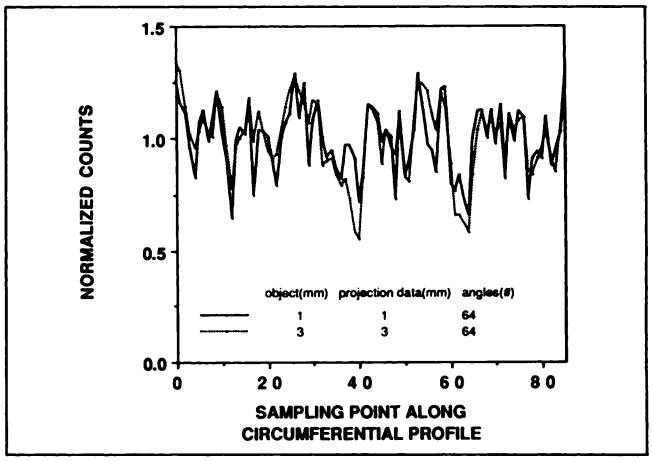

FIGURE 4. Circumferential profiles for parallel-hole reconstructed images in Figures 2 and 3.

(Fig. 2) indicates a slight blurring effect. Quantitative comparison using ROIs (Table 1; columns 1, 5) indicates good agreement for grey matter structures and slight deviations for some white matter and ventricular structures. The good agreement for the grey matter structures is also indicated in the circumferential profiles (Fig. 4). The modest deviations are due to both the resolution of the object representation (Table 1, columns 5, 6) and to the resolution of the projection sampling (Table 1; columns 1, 6). There is a negligible effect of increased angular sampling (Figs. 3, 5; Table 1; columns 1, 2). For all parallel-hole simulations described below, we used 3 × 3 × 3 mm brain model resolution with 3-mm resolution for the projection data and 64 angular views.

Simulation of Grey Matter in an Isolated Basal Ganglia Slice Using Parallel-Hole Collimators

There is some spillover of reconstructed counts into the white matter and ventricular structures, for both the highest resolution (Table 1; column 5) or the lower resolution (Table 1; column 1) simulations. The circumferential profiles for the simulated image (Fig. 4) show that an apparent approximately two-fold variation in cortical radioactivity concentration can arise from regions that are theoretically of identical radioactivity concentration.

Simulation of Grey Matter in a Basal Ganglia Slice Within a Three-Dimensional Brain Using Parallel-Hole Collimators

Circumferential profiles (Fig. 6) for an isolated brain slice (Fig. 3) and a brain slice within a three-dimensional brain (Fig. 7A) indicate that the out-of-slice contribution has little effect on the shape of the cortical radioactivity distribution. On the other hand, the absolute values were significantly different (Table 1; columns 1, 3), indicating a quantitatively large out-of-slice contribution. This large contribution is not surprising, since a thin (3 mm) slice was simulated.

Simulation of Grey and White Matter in a Basal Ganglia Slice Within a Three-Dimensional Brain Using Parallel-Hole Collimators: Imaging of the Three-Dimensional Hoffman Physical Brain Phantom

The grey-to-white matter ratio in the simulated reconstructed brain slice (Fig. 7B) is approximately 2.5:1 (Table 1; column 4) in comparison with the theoretical ratio of 5:1. For the physically imaged brain phantom (Fig. 8), the grey-to-white matter ratio is approximately 2:1 (Table 1; column 7), in comparison with the theoretical ratio of 5:1. Comparison of the shapes of the circumferential profiles (Fig. 9) and the tabulated ROI data (Table 1; columns 4, 7) for the simulated and physically imaged phantoms indicates the correspondence between the two images.

Simulation of Grey Matter in an Isolated Basal Ganglia Slice Using Point-Focusing Collimators

For the reconstructed image of the grey matter distribution in an isolated slice using point-focusing collimators (Fig. 10), there is some spillover of counts into the white matter and ventricular structures (Table 1; column 8). The

FIGURE 3. Simulated reconstructed image of grey matter in an isolated 3-mm thick basal ganglia slice imaged with parallel-hole collimators. Three-millimeter resolution was used for the object and projection data sampling and 64 angular views were utilized.

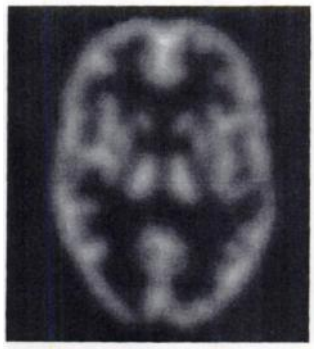

FIGURE 5. Simulated reconstructed image of grey matter in an isolated 3-mm thick basal ganglia slice imaged with parallel-hole collimators. Three-millimeter resolution was used for the object and projection data sampling and 120 angular views were utilized.

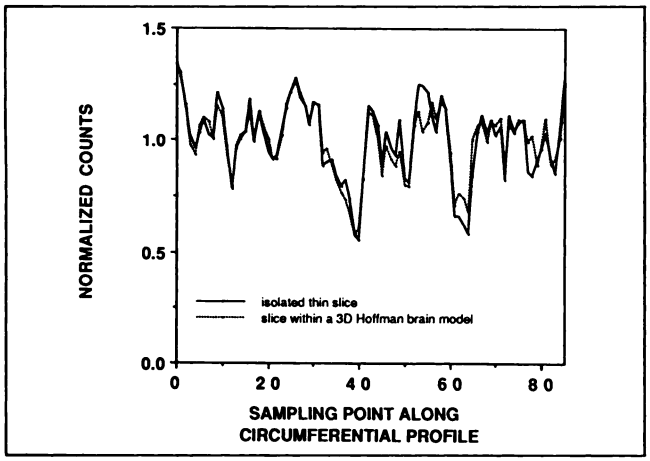

FIGURE 6. Circumferential profiles for parallel-hole reconstructed images in Figures 3 and 7A.

circumferential profile (Fig. 11) for the simulated image shows that an apparent approximately three-fold variation in cortical radioactivity concentration can arise from regions that are theoretically of identical radioactivity concentration.

Simulation of Grey Matter in a Basal Ganglia Slice Within a Three-Dimensional Brain Using Point-Focusing Collimators

Comparison of circumferential profiles (Fig. 11) for an isolated brain slice (Fig. 10) and a brain slice within a three-dimensional brain (Fig. 12A) indicate that the out-of-slice contribution has little effect on the shape of the cortical radioactivity distribution, but this effect is somewhat larger than that for parallel-hole simulations (Fig. 6). This effect with parallel-hole and point-focusing collimators can be compared quantitatively by computing the RMS errors between the isolated slice and the slice within the three-dimensional model. RMS errors, computed using profiles that all have an identical number of sampling points and whose means are all normalized to unity, are

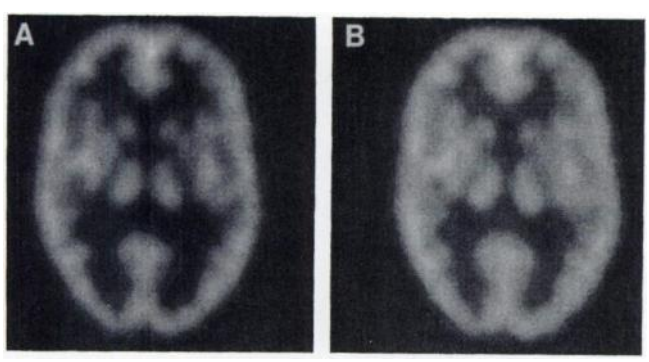

FIGURE 7. Simulated reconstructed image of grey matter (A) and grey and white matter in a 5:1 ratio (B) in a basal ganglia slice within a full three-dimensional brain model imaged with parallel-hole collimators. Three-millimeter resolution was used for the object and projection data sampling and 64 angular views were utilized.

FIGURE 8. Physically measured reconstructed image of a basal ganglia slice within the physical brain phantom imaged with parallel-hole collimators.

0.06 and 0.12 for parallel-hole and point-focusing collimators, respectively.

The absolute values were significantly different for point-focusing collimators (Table 1; columns 8, 9), indicating a quantitatively large out-of-slice contribution. This out-of-slice contribution (approximately six-fold) is larger than that for parallel-hole collimators (Table 1; columns 1, 3; approximately three-fold).

Simulation of Grey and White Matter in a Basal Ganglia Slice Within a Three-Dimensional Brain Using Point-Focusing Collimators: Imaging of the Three-Dimensional Hoffman Physical Brain Phantom

The grey-to-white matter ratio in the simulated reconstructed brain slice (Fig. 12B) is approximately 2.5:1 (Table 1; column 10) in comparison with the theoretical ratio of 5:1. For the physically imaged brain phantom (Fig. 13), the grey-to-white matter ratio is approximately 2.5:1 (Table 1; column 11) in comparison with the theoretical ratio of 5:1. The circumferential profiles (Fig. 14) and the tabulated ROI data (Table 1; columns 10, 11) for the simulated and physically imaged phantoms permits a quantitative comparison between the two images.

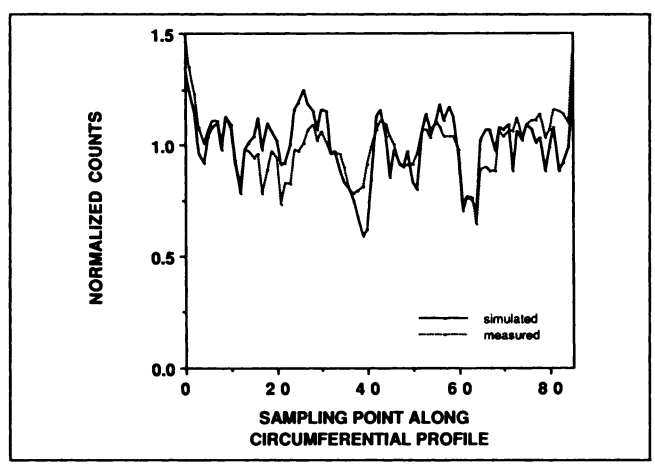

FIGURE 9. Circumferential profiles for parallel-hole reconstructed images in Figures 7B and 8.

FIGURE 10. Simulated reconstructed image of grey matter in an isolated basal ganglia slice imaged with point-focusing collimators.

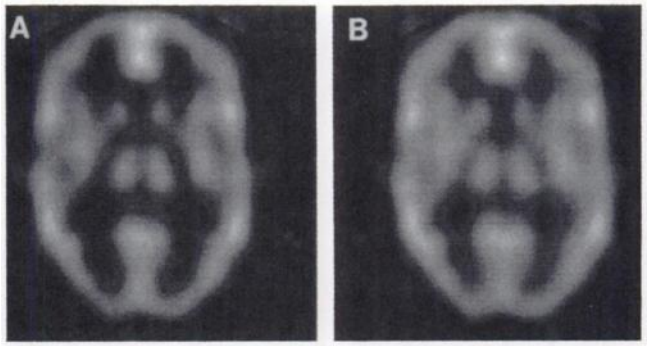

FIGURE 12. Simulated reconstructed image of grey matter (A) and grey and white matter in a 5:1 ratio (B) in a basal ganglia slice within a full three-dimensional brain model imaged with point-focusing collimators.

DISCUSSION

The simulated reconstructed images of the Hoffman three-dimensional brain model (Figs. 7B, 12B) demonstrate the qualitative degradations that might be expected in the reconstructed images of radioactivity distributed within a real brain. The simulation omitted several factors (attenuation, scatter, and noise), which degrade a real reconstruction, since one of the advantages of using simulation studies is that factors that normally act in combination in the physical process can be separately studied and each individual effect evaluated. Thus, we present these results as a baseline for future comparison with the results when attenuation, scatter, and noise will be included. This approach will allow us to develop methods for compensating for these factors and to evaluate these methods by comparison of the compensated image with the image obtained in the absence of the degrading factor.

In spite of the omission of these factors, we still report substantial deviations from the theoretical image for the simulations of neuroreceptor imaging, and it may only be of theoretical interest to determine how much further degradation occurs when these factors are included. Although the simulation (Figs. 7B, 12B) omitted these factors, there are qualitative similarities with a reconstructed image of the physically measured brain phantom (Figs. 8, 13). The circumferential profiles (Figs. 9, 14) and the ROI data (Table 1; columns 4, 7, 10, 11) derived from the simulated and physically measured brains provide a quantitative estimate of the contribution of imaging artifact to the apparent cortical deficits, particularly in the posterior parietal region. The circumferential profiles (Fig. 9, 14) show that an apparent two- to three-fold variation in regional radioactivity concentration can artifactually arise from regions that are of theoretically identical radioactivity concentration. There are significant deficits in the reconstructed image of the simulated data, although the mathematical model had no deficit. The same types of artifacts which we have demonstrated in the simulated images may also occur in the physically measured images of human subjects (*2,5,6*).

The high frequency variation in the simulated high-resolution circumferential profiles (Figs. 9, 14) is not the result of noise or statistical fluctuation, since the simulations were noise-free. As shown previously for point-focusing collimators (*5,6*), these variations are completely deterministic, and are a function of the angular position of the detectors relative to the brain slice, the three-dimensional spatial dependence of the cortical thickness, and the position and orientation of the cortical regions.

Both parallel-hole and point-focusing collimators exhibit qualitatively similar artifactual variations along the cortical circumferential profiles (Figs. 9, 14), indicating that this artifact may be a general property of SPECT

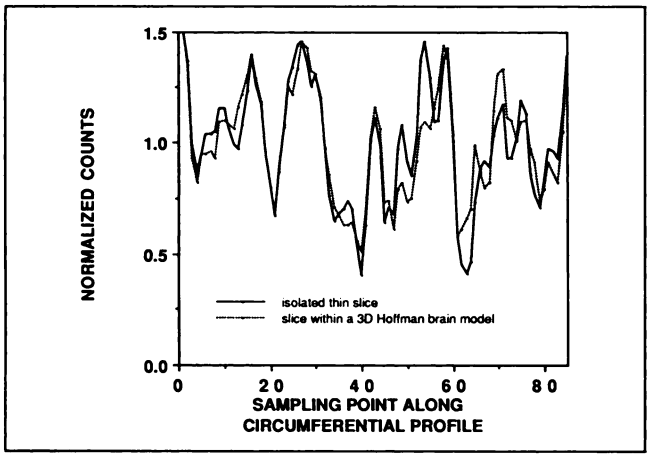

FIGURE 11. Circumferential profiles for point-focusing reconstructed images in Figures 10 and 12A.

FIGURE 13. Physically measured reconstructed image of a basal ganglia slice within the physical brain phantom imaged with point-focusing collimators.

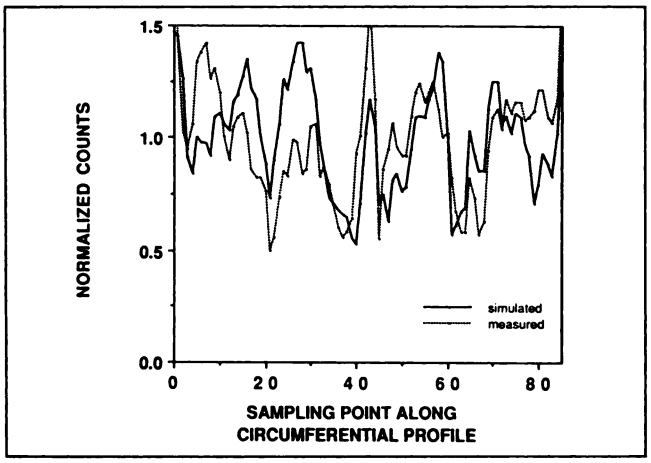

FIGURE 14. Circumferential profiles for point-focusing reconstructed images in Figures 12B and 13.

imaging, not a property of a particular imaging device. The circumferential variation is slightly greater for point-focusing than for parallel-hole collimators, but this difference is small compared to the magnitude of the overall variation. *Thus, it is clear that SPECT images represent a combination of anatomy and function, but not function alone.* The finite resolution of the imaging system imposes a limitation on our ability to measure pure function. This couples anatomy into the image in a complex nonlinear way.

We have demonstrated that the quantitative potential of SPECT for estimating the regional concentration of neuroreceptors or blood flow can be degraded as a result of finite detector resolution and inaccuracies in image reconstruction. In particular, a shape- and size-dependent recovery coefficient causes two regions with identical radioactivity concentration artifactually to appear to have significantly different radioactivity concentrations.

The major difference between parallel-hole and point-focusing collimators is the nature of the out-of-slice contribution. This distortion is both qualitative (Figs. 6, 11) and quantitative (Table 1; columns 1, 3, 8, 9). This effect will tend to diminish our ability to detect variations due to a disease state if that variation is localized within a single slice.

Comparison of the simulated reconstructed brain slice (Fig. 7B) to the physically measured phantom (Fig. 8) indicate the degree of realism of the simulation procedure. Inclusion of additional degrading factors in the simulation procedure, such as attenuation, scatter, and noise, would be expected to further improve the correspondence of the simulated image with the physically measured image.

The major limitations of the simulation procedure are: (a) the low resolution representation of the brain model that we used in order to decrease the time required for computation, and (b) the omission of additional degrading factors such as attenuation, scatter, and noise. Future studies are planned that will overcome these limitations.

Possible applications of the simulation procedure include: (a) aiding in reducing mistakes in interpreting an apparent deficit as representing a physiologic variation, and (b) utilization in a quantitatively accurate iterative reconstruction algorithm. The importance of incorporating a realistic three-dimensional model of the imaging procedure can be understood by a quotation from Parker (*12*):

"The most important part of the iterative reconstruction is the model of the data collection operation.... The model, A, of the data collection process is much more important than the reconstructor, H. Generally speaking, the reconstructor affects how rapidly the estimate approaches the correct answer, but the model of the data collection determines how accurate the reconstruction will be."

APPENDIX

COMPUTATION OF PSF FROM LSF

Assume that the PSF is given as:

$$PSF(x,y,z) = \sum_i AMP_{PSF}(i)e^{-(x^2+y^2)/2\sigma^2_{PSF}(i)}, \qquad \text{Eq. 1}$$

where $AMP_{PSF}(i) = AMP_{PSF}(i)(z,d)$, $\sigma_{PSF}(i) = \sigma_{PSF}(i)(z,d)$: z = distance, d = depth.

LSF(y,z) is defined as:

$$LSF(y,z) = \int_{-\infty}^{\infty} PSF(x,y,z)dx. \qquad \text{Eq. 2}$$

By substituting Equation 1 into Equation 2:

$$\begin{aligned} LSF(y,z) &= \sum_i \int_{-\infty}^{\infty} AMP_{PSF}(i)e^{-(x^2+y^2)/2\sigma^2_{PSF}(i)}dx \\ &= \sum_i \int_{-\infty}^{\infty} AMP_{PSF}(i)e^{-x^2/2\sigma^2_{PSF}(i)}e^{-y^2/2\sigma^2_{PSF}(i)}dx \\ &= \sum_i AMP_{PSF}(i)e^{-y^2/2\sigma^2_{PSF}(i)} \int_{-\infty}^{\infty} e^{-x^2/2\sigma^2_{PSF}(i)}dx \\ &= \sum_i AMP_{PSF}(i)\sqrt{2\pi}\,\sigma_{PSF}(i)e^{-y^2/2\sigma^2_{PSF}(i)}. \qquad \text{Eq. 3} \end{aligned}$$

Equation 3 suggests that LSF(y,z) can be modeled as:

$$LSF(y,z) = \sum_i AMP_{LSF}(i)e^{-y^2/2\sigma^2_{LSF}(i)},$$

where

$$\sigma_{LSF}(i) = \sigma_{PSF}(i) \qquad \text{Eq. 4}$$

and

$$AMP_{LSF}(i) = AMP_{PSF}(i)\sqrt{2\pi}\,\sigma_{PSF}(i). \qquad \text{Eq. 5}$$

Therefore

$$AMP_{PSF}(i) = \frac{AMP_{LSF}(i)}{\sqrt{2\pi}\,\sigma_{PSF}(i)}. \qquad \text{Eq. 6}$$

By replacing Equations 4 and 6 into Equation 1, PSF can be computed from LSF as:

$$PSF(x,y,z) = \sum_i \frac{AMP_{LSF}(i)}{\sqrt{2\pi}\ \sigma_{LSF}(i)} e^{-(x^2+y^2)/2\sigma^2_{LSF}(i)}. \qquad \text{Eq. 7}$$

ACKNOWLEDGMENTS

The authors thank Drs. Frank B. Atkins and Murray H. Loew for useful discussions and suggestions. This work was supported by a grant from the National Institutes of Health (NS22215) and, in part, by a grant from the Department of Energy (DE FG05 88ER60649).

REFERENCES

1. Holman BL, Gibson RE, Hill TC, Eckelman WC, Albert M, Reba RC. Muscarinic acetylcholine receptors in Alzheimer's disease in vivo imaging with iodine-123-labeled 3-quinuclidinyl-4-iodobenzilate and emission tomography. *JAMA* 1985;254:3063–3066.
2. Kim HJ, Zeeberg BR, Gibson RE, Hosain P, Wesley R, Reba RC. SPECT study of the localization of R,R-[^{123}I]IQNB in Alzheimer's patients and normals [Abstract]. *J Nucl Med* 1990;31:729.
3. Hoffman EJ, Huang SC, Phelps ME. Quantitation in positron emission computed tomography: 1. Effect of object size. *J Comput Assist Tomogr* 1979;3:299–308.
4. Davies P, Verth AH. Regional distribution of muscarinic acetylcholine receptor in normal and Alzheimer's-type dementia brains. *Brain Res* 1978;138:385–392.
5. Kim HJ, Zeeberg BR, Loew MH, Reba RC. 3D simulations of multidetector point-focusing SPECT imaging. *J Nucl Med* 1991;32:333–338.
6. Kim HJ, Zeeberg BR, Loew MH, Reba RC. 3D computer simulations of resolution effects of multidetector point focusing SPECT imaging. *IEEE Trans Med Imag* 1991:in press.
7. Hoffman EJ, Cutler PD, Digby WM, Mazziotta JC. 3-D phantom to simulate cerebral blood flow and metabolic images for PET. *IEEE Trans Nucl Sci* 1990;37:616–620.
8. Moore SC, Mueller SP. Inversion of the 3D Radon transform for a multidetector, point-focused SPECT brain scanner. *Phys Med Biol* 1986;31:207–221.
9. Chang LT. A method for attenuation correction in radionuclide computed tomography. *IEEE Trans Nucl Sci* 1978;NS-25:638–643.
10. SME Multi-X 810 B preliminary user's guide. Strichman Medical Equipment, Inc., Massachusetts, 1989.
11. Links JM, Loats HL, Holcomb HH, Loats SE, Stumpf MJ, Wagner HN Jr. Cortical circumferential profiling: an objective approach to cortical quantification in emission tomography [Abstract]. *J Nucl Med* 1989;30:816.
12. Parker JA. *Image reconstruction in radiology.* Boca Raton: CRC Press; 1990:480.